Front. Struct. Civ. Eng. 2016, 10(4): 394–408
DOI 10.1007/s11709-016-0352-z

RESEARCH ARTICLE

Design concepts of an aircraft wing: composite and morphing airfoil with auxetic structures

P R BUDARAPU[a,*], Sudhir Sastry Y B[c], R NATARAJAN[c]

[a] *Department of Aerospace Engineering, Indian Institute of Science, Bangalore 560 012, India*
[b] *Department of Aeronautical Engineering, College of Engineering, Defence University, Ethiopia*
[c] *Department of Aeronautical Engineering, Institute of Aeronautical Engineering, Hyderabad, India*
[*] *Corresponding author. E-mail: pattabhib@gmail.com*

ABSTRACT This paper is categorized into two parts. (1) A frame work to design the aircraft wing structure and (2) analysis of a morphing airfoil with auxetic structure. The developed design frame work in the first part is used to arrive at the sizes of the various components of an aircraft wing structure. The strength based design is adopted, where the design loads are extracted from the aerodynamic loads. The aerodynamic loads acting on a wing structure are converted to equivalent distributed loads, which are further converted point loads to arrive at the shear forces, bending and twisting moments along the wing span. Based on the estimated shear forces, bending and twisting moments, the strength based design is employed to estimate the sizes of various sections of a composite wing structure. A three dimensional numerical model of the composite wing structure has been developed and analyzed for the extreme load conditions. Glass fiber reinforced plastic material is used in the numerical analysis. The estimated natural frequencies are observed to be in the acceptable limits. Furthermore, the discussed design principles in the first part are extended to the design of a morphing airfoil with auxetic structure. The advantages of the morphing airfoil with auxetic structure are (i) larger displacement with limited straining of the components and (ii) unique deformation characteristics, which produce a theoretical in-plane Poisson's ratio of -1. Aluminum Alloy AL6061-T651 is considered in the design of all the structural elements. The compliance characteristics of the airfoil are investigated through a numerical model. The numerical results are observed to be in close agreement with the experimental results in the literature.

KEYWORDS wing design, aerodynamic loads, morphing airfoil, auxetic structures, negative Poisson's ratio

1 Introduction

The ever increasing demand for light and efficient structures has led the engineers and scientists to use the composite materials in achieving superior performance with unique thermo-mechanical properties and specific strengths, which are not possible with the traditional materials Frolov [1]. The strength to weight ratio of composite materials is superior compared to the conventional aluminum alloys. In particular, the use of laminated polymeric composites has many potential applications in a variety of engineering fields: for example, in the aircraft structures Budarapu et al. [2–4] armoured vehicles Benloulo and Sánchez-Gálvez [5] and space vehicles Rawal [6], to name a few. Therefore, composite materials are the most suitable materials in the aerospace industry, where the strength to weight ratio is the prime factor.

On the other hand, amorphing aircraft is an aircraft containing multi-point adaptability, probably incorporating macro, micro, structural and/or fluidic approaches for the control. The word 'morphing' refers to seamless shape changes that are continuous and not to classical discrete aircraft wing adaptation systems, such as flaps or leading and trailing-edge high-lift devices. Therefore, morphing aircraft changes its shape and size during the flight. The concept of morphing is directly inspired by the nature.

Gliding birds continually change the shape and size of their wings Tucker [7], probably to exploit the profound effect of wing morphology on aerodynamic performance Weiss [8]. Swifts (Apus apus) are some of the most

Article history: Received Jan 12, 2016; Accepted Apr 29, 2016

efficient birds in active flying by flapping the wings, instead of just gliding Lentink et al. [9]. They spend nearly their entire life time in the air. Flying slowly with extended wings gives swifts maximum flight efficiency. Swept wings will deliver a superior aerodynamic performance for flying fast and straight; Extended wings are superior for slow glides and turns. This superiority is due to better aerodynamic performance with the exception of fast turns Lentink et al. [9]. Swept wings are better for fast and tight turns since they do not break easily as compared to the extended wings. Swept wings are less effective at generating lift while turning at high speeds, but can bear the extreme loads. Since the birds possess an articulated skeleton under muscular control, their wings lend themselves to morphing. Also the changing overlap between feathers allows continuous changes in wing shape and size. Gliding birds sweep their hand-wings back at high flight speeds Parrott [10], and spread their wings in turns Newman [11]. Therefore, morphing airfoil is a concept evolved from the flight mechanics of the birds. Recently, McGowan et al. McGowan et al. [12] have introduced the smart materials, adaptive structures, micro flow control, biomimetic concepts, optimization and controls in the morphing technology. This has opened opportunities to implement novel structural morphing concepts in the aerospace industry.

In general, morphing requires structural compliance which often conflicts with the stiffness requirements of the prescribed aerodynamic loads. The belt rib concept Campanile and Sachau [13] allows the achievement of continuous camber variations by transferring the stroke of an actuator to a geometric shape change of the airfoil through a closed belt and an internal structural network. The finger concept Monner et al. [14] is a similar solution for camber variation, where the airfoil features a flexible rib composed of plate-like elements connected through revolute joints. In helicopter blades tension-torsion coupling Bueter et al. [15] has been employed as an effective means to actively control camber. The airfoil structures Cadogan et al. [16], the variable-span morphing wings Bae et al. [17]; Trenker [18] and the hinge-less flexible leading and trailing edges actuated using shape memory alloys Kudva [19], are among the other design solutions for morphing. The auxetic structure can be accommodated within an airfoil, so that its compliant characteristics can be used to achieve chord wise bending Spadoni et al. [20]. The deformation mechanisms of auxetic structures allow continuous deformations of the airfoil to occur with all the individual members undergoing strains within the linear range of the material. The ability to sustain large deformations without exceeding yield conditions is required to achieve repeatability, while smooth deformations are required for aerodynamic efficiency.

The strength to weight ratio of composite materials is superior compared to the conventional aluminum alloys. Therefore, composite materials are widely used in the aerospace industry. Refer Budarapu et al. [3] for the aeroelastic analysis of stiffened composite wing structure. The performance can be further improved by covering the wing structure a layer of carbon nanotubes embedded in an elastic medium Budarapu et al. [4]. Recently, due to the superior mechanical properties and multifunctional characteristics, cellular materials are used in the design of structural components. Their properties are topology dependent, i.e., they are a function of the geometry and of the shape of the elementary cell composing the assembly. Cell shape and geometry can be tailored to satisfy requirements of a given application or to achieve various functionalities.

Techniques based on the continuum mechanics principles Budarapu et al. [2]; Thai et al. [21] are frequently used for a wide range of composite applications to formulate the basic governing equations. However, continuum mechanics is restricted to laminates with simple geometries and behavior. More sophisticated models Nguyen-Xuan et al. [22]; Phan-Dao et al. [23] have been developed by adopting contact interaction Kerfriden et al. [24] algorithms within a finite element (FE) procedure for simulation of the debonding behavior. There are several advanced techniques to model the continuum Amiri et al. [25,26]; Areias and Rabczuk [27]; Areias et al. [28–30]; Belytschko et al. [31]; Bordas et al. [32–34]; Budarapu et al. [35–37]; Cai et al. [38,39]; Ghorashi et al. [40]; Liu and YT. [41]; Nguyen-Thanh et al. [42]; Rabczuk et al. [43–53]; Talebi et al. [54–56]; Yang et al. [57]; Zhuang et al. [58–60]; Zi et al. [61], to name a few. However, analytical techniques to model the laminated composites are not viable from the design point of view, due to the involvement of large number of variables. Therefore, the present work focuses on the design and analysis of the composite wing structure. A three-dimensional Finite Element Model of the composite wing, has been developed to perform the vibrational analysis. Also numerical analysis of a morphing airfoil with auxetic structures have been performed to investigate the compliance of the proposed configuration. The results of the numerical analysis are validated with experimental results in the literature.

The arrangement of the article is as follows: The design procedure is explained in Section 2. Estimation of the sizes of the spars, ribs and the skin are discussed in Section 2.3. Design procedure of the auxetic wing structure are discussed in Section 3. Section 4 is devoted for the finite element analysis of the three dimensional full scale composite and auxetic wing structures through three numerical examples. The key contributions are summarized in Section 5.

2 Design procedure

The main function of a wing structure is to pick up the air

loads and transfer them to fuselage. The wing as a whole performs the combined function of a beam and a torsion member. It consists of axial members in stringers, bending members in spars and shear panels in cover skin and webs of spars Ainsworth et al. [62]. The spar is a heavy beam running span wise to take transverse shear loads and span wise bending Morishima [63]. Wing ribs are planar structures capable of carrying in-plane loads and are placed chord wise along the wingspan Arunkumar et al. [64]. Besides serving as load re-distributers, ribs also hold the skin stringer to the designed contour shape. Ribs reduce the effective buckling length of the stringer skin system and thus increase their compressive load capability. The cover skin of the wing together with the spar webs form an efficient torsion member Kennedy and Martins [65]. For subsonic airfoils, the skin is relatively thin and may be designed to undergo post buckling Sudhir et al. [66–68]. Refer to Budarapu et al. [3] for an aero-elastic analysis of stiffened composite wing structure.

The aerodynamic loads on a typical wing structures for different operating conditions A, C, D and P are listed in Table 1. The load condition 'C' is considered in the present wing design. Glass Fiber Reinforced Plastic (GFRP) material with mechanical properties as listed in Table 2 are considered in the design of the composite wing structure.

Table 1 Typical operating loads experienced by an UAV wing structure

load case	EAS speed (kmph)	Mach number	load factor
A	651.0	0.518	6.716
C	942.4	0.750	6.716
D	1068.0	0.850	5.034
P	1068.0	0.850	5.340

Table 2 Mechanical properties of GFRP considered in the present design Jones [69]; Reddy [70]

quantity	units	GFRP
bending strength- Tensile	MPa	250
bending strength- Compression	MPa	150
shear strength	MPa	40
Young's modulus in the warp direction	MPa	20000
Young's modulus in wept direction	MPa	20000
shear modulus	MPa	3000
density	Kg/m^3	1800
Poisson's ratio	none	0.3

2.1 Estimation of shear forces

Due to the symmetry of the wing structure we considered the semi-wing in the design calculations. The semi-wing can be approximated as a cantilever, whose fixed end is attached to the fuselage. Geometric details of the wing structure like chord length, span, area, leading edge and mean aerodynamic chord are mentioned in Table 3. The aerodynamic pressure loads at different stations across the chord are converted to the span wise distributed loads per unit length. Typical pattern of the distributed loads along the length of the wing is shown in Fig. 1. Lift force is the major load acting on the wing structure apart from the self weight of the wing and the weight of the fuel. From Fig. 1, the distribution of the uniformly distributed load along the wing span is observed to be nonlinear. Knowing the distribution of loads along the length, shear forces at various sections can be arrived by multiplying the section length and cumulatively adding the forces on preceding sections, as given below

Table 3 Typical operating loads experienced by an UAV wing structure

Sr. No.	detail	units	value
1	center line chord	m	1.2250
2	span	m	3.0000
3	area	m^2	2.2695
4	mean aerodynamic chord (MAC)	m	0.8532
5	location of LE from nose		
	(a) center line chord	m	2.6850
	(b) MAC	m	3.0568
6	location of LE and $c/4$ point above FRL		
	(a) center line chord	m	−0.3025
	(b) MAC	m	−0.3025

Knowing the distribution of loads along the length of the wing, shear forces at various sections can be arrived by multiplying the section length and cumulatively adding the forces on preceding sections, as given below:

$$V(x) = \int q(x)\mathrm{d}x, \tag{1}$$

where $q(x)$ is the load distribution per unit length, mentioned in Fig. 1. Therefore, the shear force distribution estimated using Eq. (1), for all the load cases is plotted in Fig. 2. From Fig. 2 the shear forces are decreasing with the speed. This is because the coefficient of lift drastically decreases for Mach numbers greater than 1. Therefore, the lift force and hence the shear forces on the wing structure continuously decreases with increasing speeds.

2.2 Estimation of bending and twisting moments

Bending moment can be estimated by integrating shear force expression in Eq. (1):

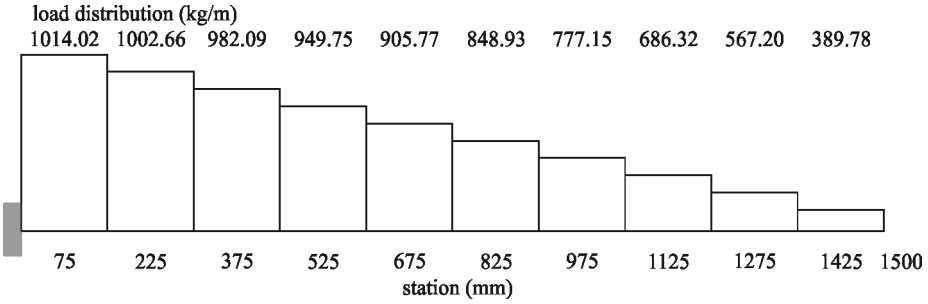

Fig. 1 Load distribution at different sections for load case "C" mentioned in Table 1

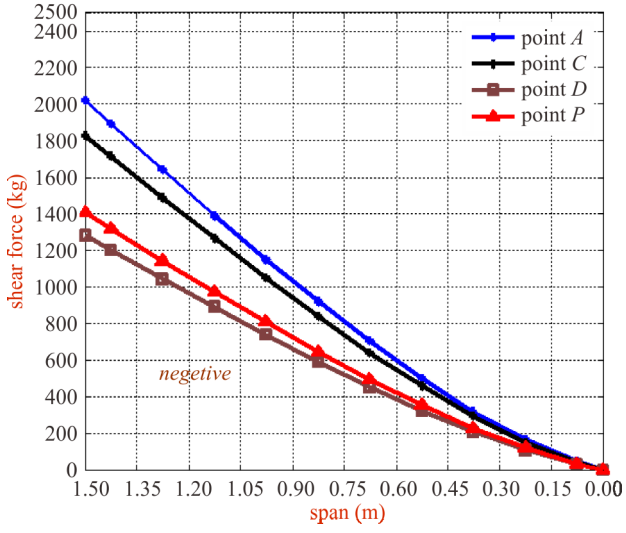

Fig. 2 Distribution of shear force for all the load cases mentioned in Table 1

$$M(x) = \int V(x)\mathrm{d}x. \tag{2}$$

To estimate the bending loads the uniformly distributed loads in Fig. 1 are first converted to point loads based on the span of the load, as shown in Fig. 3. Note that a factor of safety of 1.5 is assumed to obtain the design loads in Fig. 3. Therefore, the bending moment at any given section distance x from the wing tip, can be estimated by

$$M = 87.7(x-0.075) + 127.62(x-(0.075+0.15)). \tag{3}$$

The above procedure is extended further to estimate the bending moments at all the stations. Twisting moment is estimated from the lift force and the distance between the center of pressure and aerodynamic center as:

$$\mathrm{TM} = LF * d_{CPAC}, \tag{4}$$

where TM is the twisting moment, LF is the Lift force and d_{CPAC} is the distance between the center of pressure and aerodynamic center. The Lift Force can be obtained from the area under the load distribution curve. The center of pressure (CP) line can be estimated as:

$$y_{cp} = \frac{\sum \Delta pL}{\sum \Delta p}, \tag{5}$$

where L is the distance between two pressure load points along the chord and Δp is the pressure distribution across the chord at a particular station. CP values at different sections can be calculated by using Eq. (5). The center of pressure line can be obtained by joining all the center of pressure points. One such line for load case "C" is shown in Fig. 4. Figure 4 also shows the chord lines at 20% and 65% chord lengths apart from the CP line. The aerodynamic center (AC) line is assumed at 45% of chord length, as plotted in Fig. 4. Therefore, the twisting moment can now be estimated using Eq. (4). Variation of the bending and the twisting moments with span for all the load cases are plotted in Figs. 5(a) and (b), respectively.

2.3 Estimation of the sizes of spars, ribs and the skin

After knowing the shear forces, bending and twisting moments, the sizes of various sections can be estimated for the given material from the strength based design. In the strength based design, the material design is based on the failure loads. The following assumptions are adopted in the design calculations. Webs are the vertical members in a

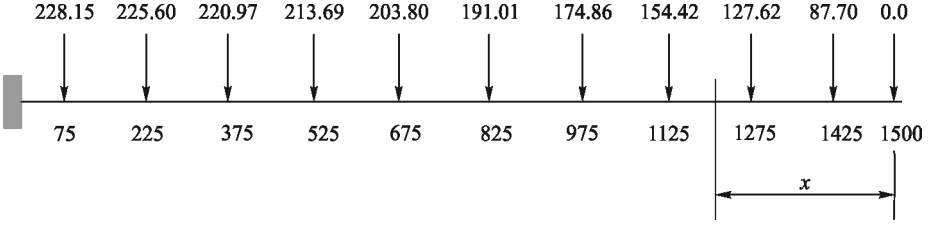

Fig. 3 Conversion of the distributed loads in Fig. 1 into design loads (kg) at various sections for the load case "C" mentioned in Table 1

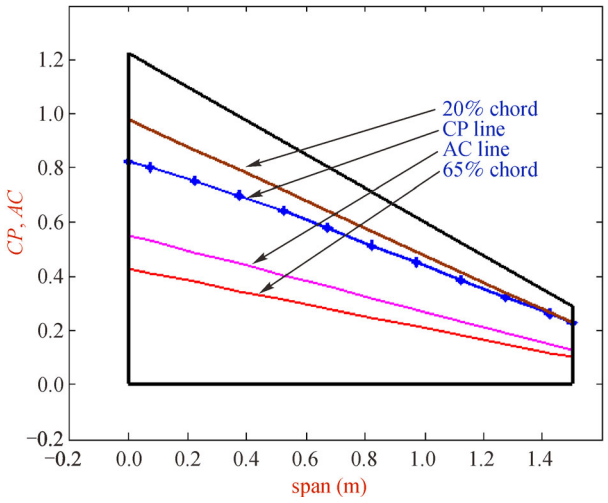

Fig. 4 CP line and Aerodynamic Center line for the load case "C" mentioned in Table 1

section, which take the direct transverse loads. Flanges are the flat members which absorbs the shear loads due to bending and twisting moments. The in-plane shear loads are resisted by the skin. Three stringers on top and three at the bottom are considered in the present design as shown in Fig. 6. The stringers are equally spaced between the spars. Cross section of the stringers is assumed to be a hat section. Whereas, rectangular tube sections are considered for spars. Both stringers and spars are proposed to be continuous structures. GFRP material with the mechanical properties listed in Table 2 are adopted in all the calculations.

Based on the above mentioned considerations and following the strength based design, the estimated sizes of spars, stringers, ribs and the skin are reported in Tables 4 and 5. Variables w_{flange} and t_{flange} in Table 4 indicate the width and thickness of the flange, respectively. The corresponding variables for the web are denoted by w_{web} and t_{web}, respectively. Similarly the width and thickness of the skin in Table 5 are denoted by w_{skin} and t_{skin} and that of leading edge (LE) and trailing edge (TE) are indicated by w_{LE} and t_{LE}; and w_{TE} and t_{TE}, respectively. The thickness of the rib in Table 5 is represented by t_{rib}. Note that a minimum of 1.25 mm thickness is ensured for easy manufacturing. Based on Tables 4 and 5, the sizes of all the components are gradually decreasing with the span, starting from the fixed end. This is because the loads are maximum at the fixed end and reduces to zero at the tip of the wing.

3 Design of a morphing airfoil with auxetic structures

When the speed is approximately constant, glides can be approximated as "equilibrium gliding," encompasing turns

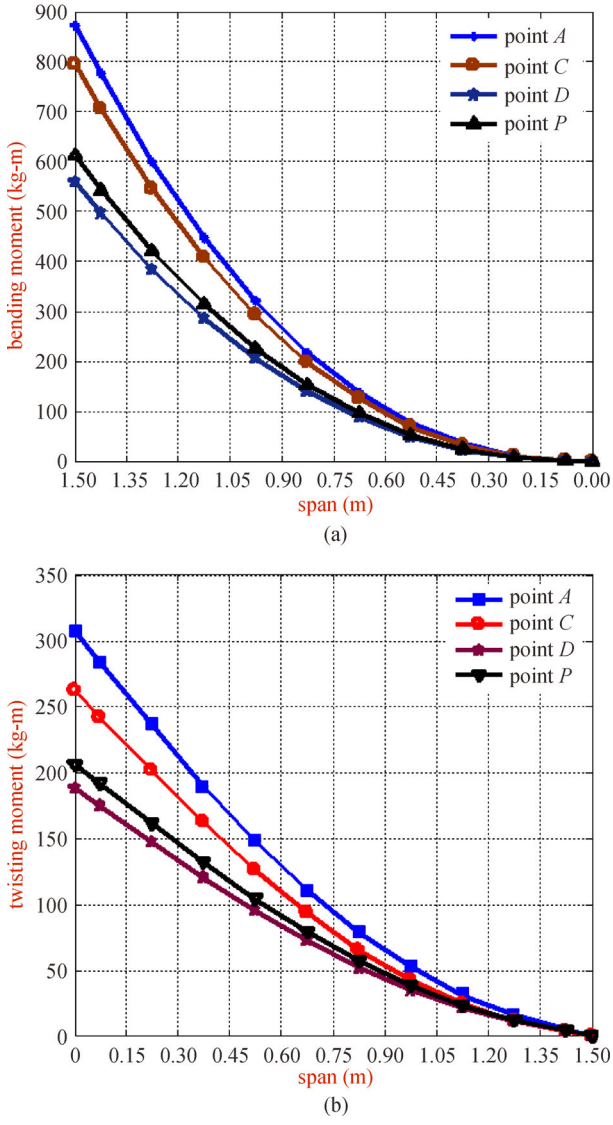

Fig. 5 Variation of the (a) bending moment and (b) twisting moment with span for all the load cases mentioned in Table 1

(with infinite radius) and straight glides. Gliding at equilibrium along a helical path is explained in Fig. 7. Figure 7(a) shows the drag and lift forces, the direction of motion and the weight of a swift in flight. As shown in Fig. 7(b), turning swifts glide at a constant glide speed, whereas glide velocity (V) changes direction along a helical path, which is inclined downward at glide angle γ. To turn without side slip, swifts incline sideways at bank angle μ. Glide angle is determined by the tangential component of lift ($\cos\mu \times L$) divided by the drag force (D). The centripetal force required for turning $\sin\mu$ component of lift ($\sin\mu \times L$). During the steady-state, flight performance can be deduced from four parameters, namely: aerodynamic lift, drag, flight velocity and body-weight, refer to Fig. 7(a). Aerodynamic force is proportional to force coefficient × square of glide speed × wing area. Swifts control force coefficient by altering wing

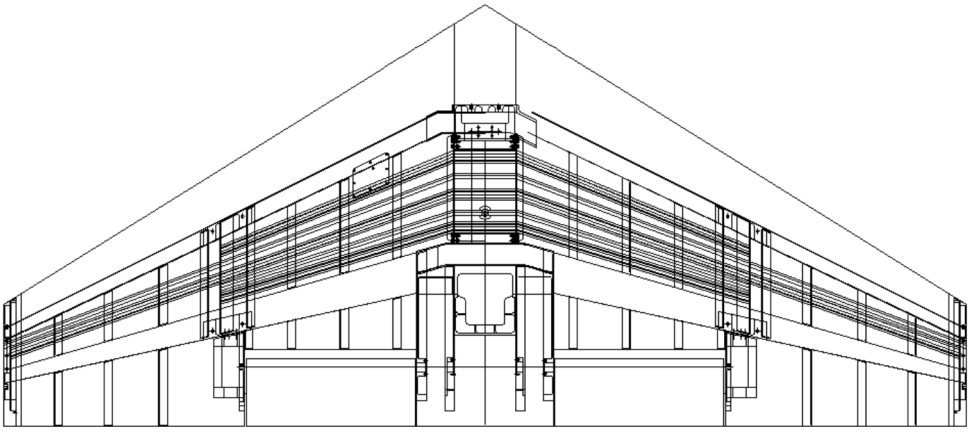

Fig. 6 Two dimensional layout of the proposed composite wing structure

Table 4 Spar sizing. Variables w_{flange} and t_{flange} indicate the width and thickness of the flange, respectively. The corresponding variables for the web are denoted by w_{web} and t_{web}, respectively

Sr. No.	$dist_{tip}$ (mm)	front spar (mm)			rear spar (mm)		
		w_{flange}	t_{flange}	t_{web}	w_{flange}	t_{flange}	t_{web}
1	1500	60.0	1.25	3.00	147.0	1.25	2.14
2	1425	60.0	1.25	2.93	141.4	1.25	2.10
3	1275	58.4	1.25	2.77	130.0	1.25	1.97
4	1125	118.9	1.25	2.58	118.9	1.25	1.84
5	975	107.6	1.25	2.37	107.6	1.25	1.70
6	825	96.4	1.25	2.13	96.4	1.25	1.52
7	675	85.2	1.25	1.85	85.2	1.25	1.32
8	525	73.9	1.25	1.53	73.9	1.25	1.10
9	375	62.7	1.25	1.17	62.7	1.25	0.84
10	225	51.4	1.25	0.75	51.4	1.25	0.53
11	75	39.9	1.25	0.29	39.9	1.25	0.21

Table 5 Sizing of ribs and the skin

Sr. No.	$dist_{tip}$ (mm)	w_{skin} b/n spars (mm)	t_{skin} (mm)	w_{LE} (mm)	t_{LE} (mm)	w_{TE} (mm)	t_{TE} (mm)	t_{rib} (mm)
1	1500	196.00	1.25	245.00	490.00	4.50	1.25	5.03
2	1425	188.50	1.25	235.63	471.26	4.00	1.25	4.90
3	1275	173.37	1.25	216.72	433.44	3.50	1.25	4.62
4	1125	158.52	1.25	198.15	396.30	3.25	1.25	4.30
5	975	143.53	1.25	179.41	358.82	2.75	1.25	3.93
6	825	128.54	1.25	160.68	321.36	2.25	1.25	3.52
7	675	113.55	1.25	141.94	283.88	1.75	1.25	3.04
8	525	98.56	1.25	123.20	246.40	1.25	1.25	2.50
9	375	83.57	1.25	104.46	208.92	1.25	1.25	1.89
10	225	68.58	1.25	85.73	171.45	1.25	1.25	1.19
11	75	53.17	1.25	66.46	132.93	1.25	1.25	0.44

shape, angle of attack, and speed. It is observed that by increasing the sweep angle from 5° to 50°, the wing aspect ratio (area to shape) decreases approximately by one third Lentink et al. [9].

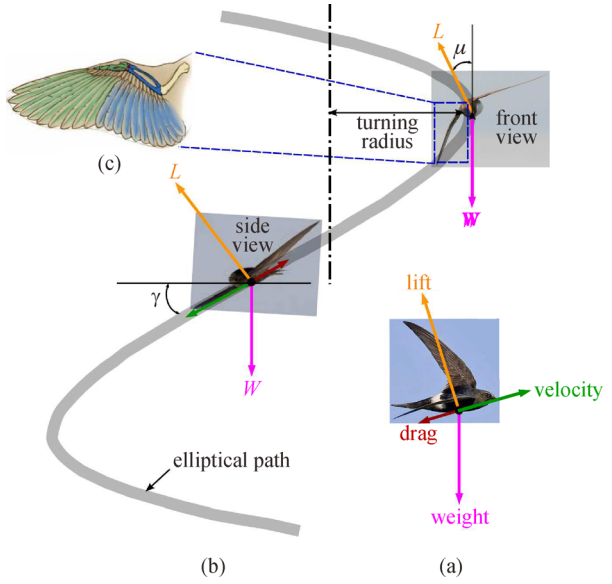

Fig. 7 Swift gliding at equilibrium. (a) Main forces acting on a swift gliding at a given velocity; (b) turning swift gliding, where L is the lift force, D is the drag force and W is the weight of the swift; (c) skeleton covered with feathers in swept and extended wing of a swift

Based on the motivation in the previous paragraph, the objective is to increase the lift force and hence the aerodynamic performance of the airfoil. The lift force can be increased by changing the swept area and the shape of the airfoil. The coefficient of lift is defined as

$$C_L = \frac{L}{\frac{1}{2}\rho v^2 S} = \frac{L}{qS}, \tag{6}$$

where L is the lift force, ρ is fluid density, v is air speed, S is planform area and $q = \frac{1}{2}\rho v^2$ is the fluid dynamic pressure. Now we define the section lift coefficient (c_l) for a two-dimensional flow over a wing of infinite span with uniform cross-section (so that the lift is independent of spanwise effects) as the lift force per unit span of the wing, i.e.,

$$c_l = \frac{1}{\frac{1}{2}\rho v^2 c}, \tag{7}$$

where c is the chord of the airfoil. Therefore, the sectional lift coefficient can be improved by changing the camber of the airfoil. However, it is advantageous to morph the camber geometry for the given angle of attack, so that the sectional lift coefficient is increased. The optimum camber geometry can be arrived by estimating the pressure difference between the top and bottom surfaces of the airfoil. Therefore, the morphed airfoil has a higher coefficient of lift for the given angle of attack, as compared to the symmetric rigid airfoil. As a result the slope of the lift coefficient versus the angle of attack curve increases, improving the aerodynamic performance.

3.1 Deformation mechanisms of the auxetic structures

A material possessing negative Poisson's ratio is known as auxetic material, see Fig. 8. Auxetic topologies represent an appealing solution for the deformable internal frame of morphing structures. An auxetic material expands in all directions under the tensile loads, as shown in Fig. 8(a) and reduce in all directions under the compressive loads as shown in Fig. 8(b). This unique property is achieved as a result of the micro scale mechanisms.

In the auxetic materials, the longitudinal extension strain in the direction of tensile load is very large compared to the transverse contraction strain. Therefore, the structure will possess a negative Poisson's ratio close to -1. The negative Poisson's ratio helps in improving the Shear modulus ($G = E/2(1 + v)$, where v is the Poisson's ratio) and hence resisting the structural deformation of the unit cells, see Fig. 9(c). We define a unit cell as the smallest repeatable structural unit. Also, a node/cell is defined as the smallest closed unit in the unit cell and the nodes are connected by ligaments. The negative Poisson's effect increases with the increase in the thickness of the ligament and node. The auxetic materials are madeup of foams, ceramics, composites or polymers. Auxetic effects occur naturally in cow teat skin and cat skin.

The mechanical behavior for the overall honeycomb structure (refer Figs. 9(a) and (b)) is based on the behavior of the unit cell structure, see Fig. 9(c). The unit cell is represented by the thicker lines in Fig. 9(c), the honeycomb is viewed as a lattice of many such unit cells. In the initial undeformed configuration, the ligaments are straight. Let a uniaxial stress, s1 or s2 is applied to the cell along horizontal or veritical direction, respectively. This results in a torque T, as shown in Fig. 9(d), which leads to bending of the ligaments and rotation of the nodes as shown Fig. 10. Figures 10(a) and (b) show the finite element models of the elliptical and circular cells, respectively. The ligament bending and the rotation of the nodes for the elliptical and circular cells can be seen in Figs. 10(c) and (d), respectively. The ligaments remain rigidly tangent to the node. Therefore, the deformation is constrained to correspond to a change of area without change of shape. Deformations due to axial compression and shear within the ligament can be neglected so long as the ligaments are sufficiently slender. Hence, the relative density of the structure is kept below a critical value Prall and Lakes [71]. Refer Prall and Lakes [71] for details on predicting the Poisson's ratios and in-plane moduli.

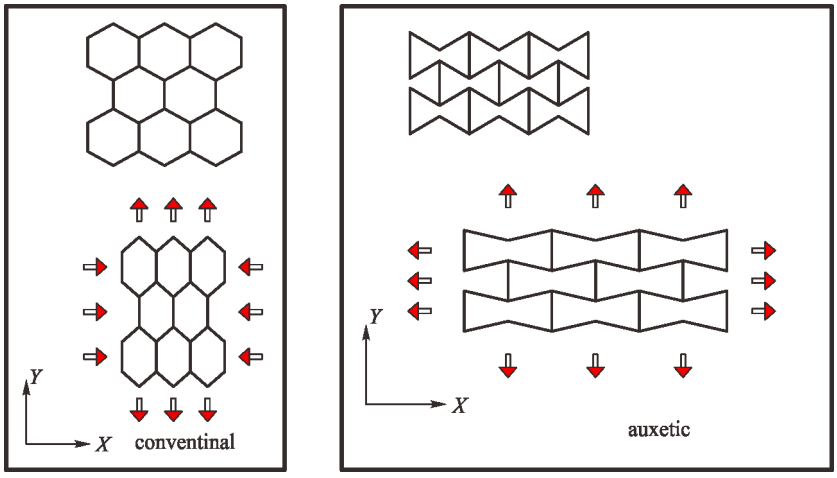

Fig. 8 (a) Non auxetic honey comb structure with positive Poisson's ratio. (b) Auxetic structure with negative Poisson's ratio

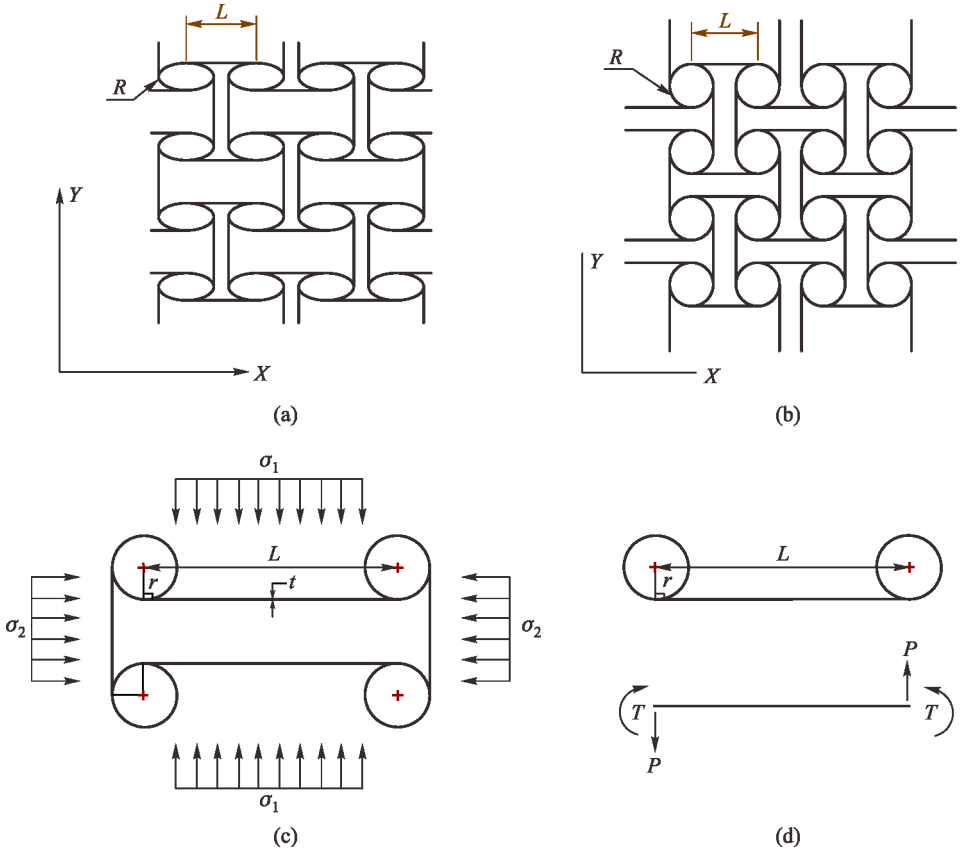

Fig. 9 Auxetic structures considered for the design. Schematics of (a) elliptical and (b) circularcells. Schematic of a unit cell geometry with (c) circular nodes, along with the loads and (d) free body diagram of a ligament in (c)

3.2 Modeling aspects of the morphing airfoil

In this paper, two types of auxetic airfoils are considered: (i) auxetic airfoil with elliptical cells (AAEC), shown in Fig. 11(a) and (ii) auxetic airfoil with circular cells (AACC), shown in Fig. 11(b). Auxetic geometry is based on a non centro symmetric topology. Auxetic topologies offers design flexibility by changing the geometrical parameters as well as the ligament thickness and material, which in turn will allow the regulation of structural

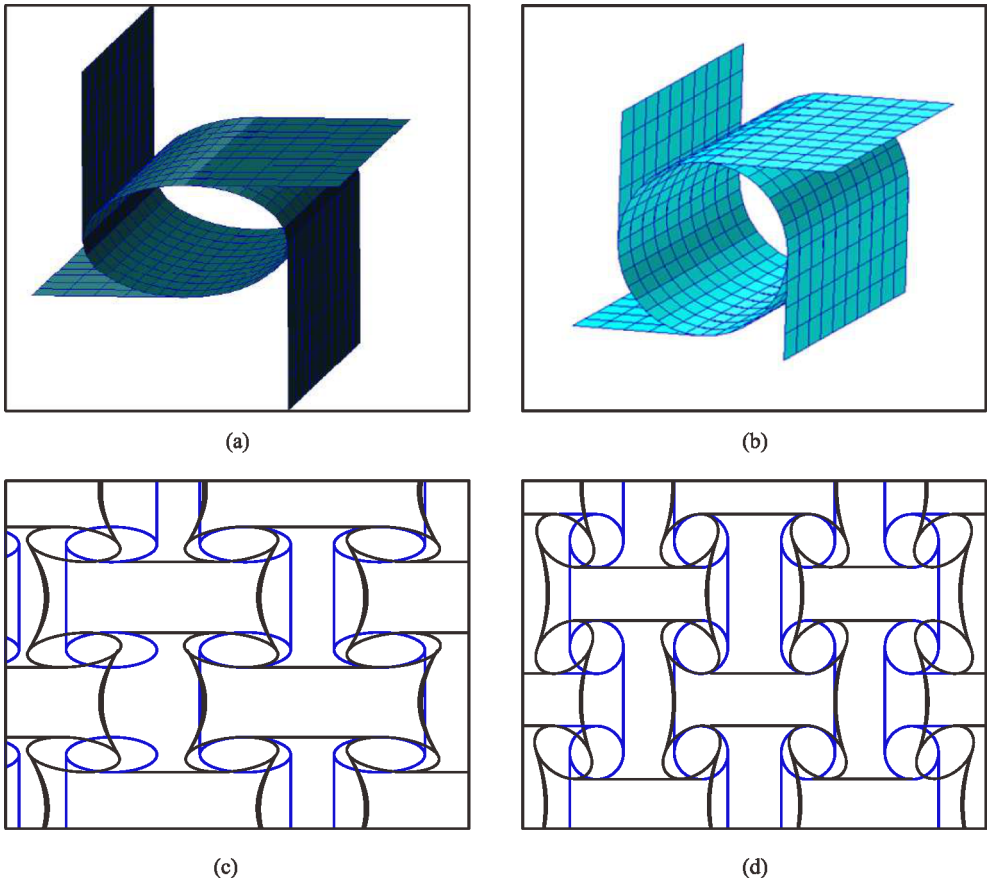

Fig. 10 Finite element models of (a) circular and (b) elliptical, cells. Deformed configuration of the auxetic structure under tensile loads, with (c) elliptical and (d) circular cells

compliance to meet various morphing behaviors and global stiffness requirements. The auxetic networks are obtained by the assembly of cells/nodes (elliptical/circular) connected by ribs/ligaments tangential to the nodes. Figures 12(a) and (b) shows the developed FE model AAEC and AACC, respectively. The numerical models are developed based on following design guidelines:

1) The root section of the wing is joined to the supporting structure through two constraint points separated chord wise. Kinematically, the two constraint points acts as hinges.

2) A flexible skin is adopted to provide adequate compliance, which allows large deformations without plastic deformation or fracture.

3) The internal structural frame is designed to take the aerodynamic loads and to provide sufficient flexural and torsional stiffness to the wing structure. The leading and trailing edge regions are made of solid material. Therefore they offer a rigid boundary conditions on the auxetic structure in the middle.

4 Numerical examples

In the present work, we consider the GFRP material in the design of a composite wing structure presented in the first example and Eppler 420 airfoil (e420-il, see Fig. 11) madeup of AL6061- T651, a 6000 series aluminum alloy,

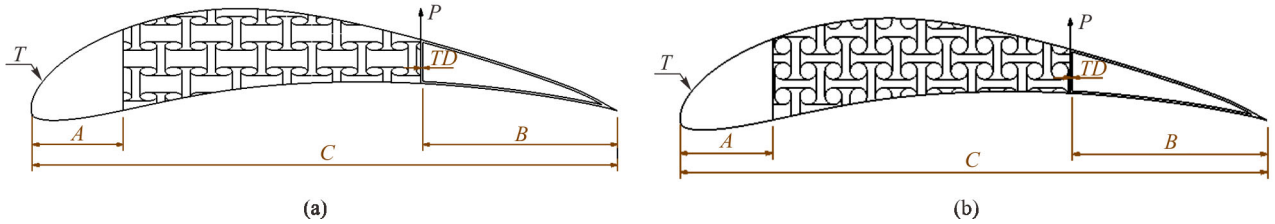

Fig. 11 Airfoil with auxetic structure of (b) elliptical cells and (b) circular cells, with chord (C) = 700 mm, A = 110 mm, B = 235 mm and skin thickness T = 1 mm

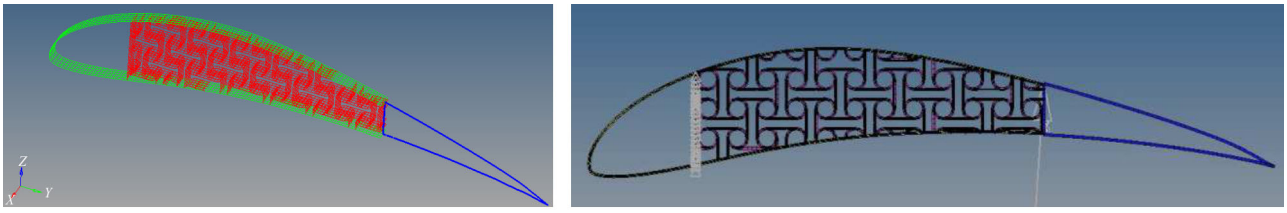

(a) (b)

Fig. 12 Finite element model of the airfoil with auxetic structures of (a) elliptical cells and (b) circular cells

in the design of the morphing airfoil with auxetic structure discussed in the second and third examples. The airfoil structures with elliptic and circular cells are shown in Figs. 11(a) and (b), respectively. The 6000 series aluminum are alloyed with magnesium and silicon, are easy to machine and can be precipitation hardened. They have good machinability and posses good resistance. They are used in the production of aircraft wing and fuselage structures.

4.1 Example1: FE modeling of composite wing structure

Based on the estimated sizes of various components of the wing structure in Section 2.3, a two dimensional layout of the composite wing is developed as shown in Fig. 6. Later on, the two dimensional layout in Fig. 6 was converted to three dimensional full scale model using the Solidworks modeling software. The developed three dimensional model of the wing structure is shown in Fig. 13(a). The three dimensional model of the wing in Fig. 13(a), was imported to Hypermesh, a finite element meshing software to carry out the meshing operation. The element sizes are carefully adjusted depending on the size and the criticality of a particular component. The completely meshed model of the wing is shown in Fig. 13(b). The meshed leading edge, skin, ribs and spars can be seen in Fig. 13(a). Free-Free boundary conditions are imposed on the wing and the Normal Modes analysis is performed in the commercial finite element software MSc. Nastran. The first five natural frequencies of the composite wing are estimated as 43.57, 71.68, 96.55, 135.11 and 153.66 Hz. Deformed configurations corresponding to the first two modes are plotted in Figs. 13(c) and (d), respectively. Based on Figs. 13(c) and (d), the first two modes are observed to be bending modes.

4.2 Example 2: auxetic structure with elliptic cells

In this example, the design and analysis of AAEC as shown in Fig. 11(a) is studied. Figure 12(a) shows the FE model of the AAEC. The configuration of the core is defined by selecting a periodic, two-dimensional auxetic structure with specified number of cells and L/R ratio, refer to Figs. 9(a) and (b). The resulting geometry is then mapped to the airfoil profile (Eppler 420) through the coordinate transformation. The geometric details of the airfoil structure are: chord length (C) = 700 mm, A = 110 mm, B = 235 mm, skin thickness t = 1 mm, the out-of-plane thickness = 19 mm and the trailing-edge profile (TD) = 2.54 mm. The ability to carry shear loads and the torsional rigidity of the design due to the negative Poisson's ratio suggest that the classic closed section with stressed skin is not required Spadoni et al. [20]. In fact, the core itself will provide the sufficient torsional and shear load carrying capacity. Hence, the skins would only be used to provide the surface continuity based on the aerodynamic requirements. Therefore, the application of flexible skins that are able to conform to the airfoil to allow the decambering deflections while maintaining smoothness of the airfoil surface, need to be investigated.

The mesh size is decided based on the aspect ratio and the radius of curvature. The segment of the airfoil is meshed with CQUAD4, CTRIA3 and CBEAM elements. The mesh is refined at critical locations with triangular elements at the interfaces. The skin and the auxetic core are meshed with CQUAD4 elements while the trailing edges are meshed with CBEAM elements. In the present FE model of the AAEC, there are 55945 grid points, 4991 CQUAD4 elements and 150 CBEAM elements in total. The following material properties of 6061-T651 are adopted in the FE model: Young's modulus (E) = 69 GPa, Poison's ratio (μ) = 0.33, yield strength (σ_y) = 276 MPa, tangent modulus (E_t) = 100 MPa, density (ρ) = 2700 kg/m^3. To allow the decambering deformations, the upper and lower portions of the airfoil are modeled as soft material with stiffness 100 times lower than that of the core. The leading edge region is considered to be completely clamped.

The axial load (P) is applied to the near the core as a concentrated load as show in Fig. 11(a). The load-displacement data has been generated based on the deformation configurations of AAEC and AACC at the end of the simulation, with a starting axial load of 5 N, followed by 10-150N at an interval of 10N. The deformed configurations and the distribution of the von-Mises stress of AAEC at axial loads of 5 and 50 N are plotted in Fig. 14. Figures 14(a)–(b) shows the deformed configurations and the Fig. 14(c)–(d) shows the distribution of the von-Mises stress at axial loads of 5 and 50 N, respectively. The

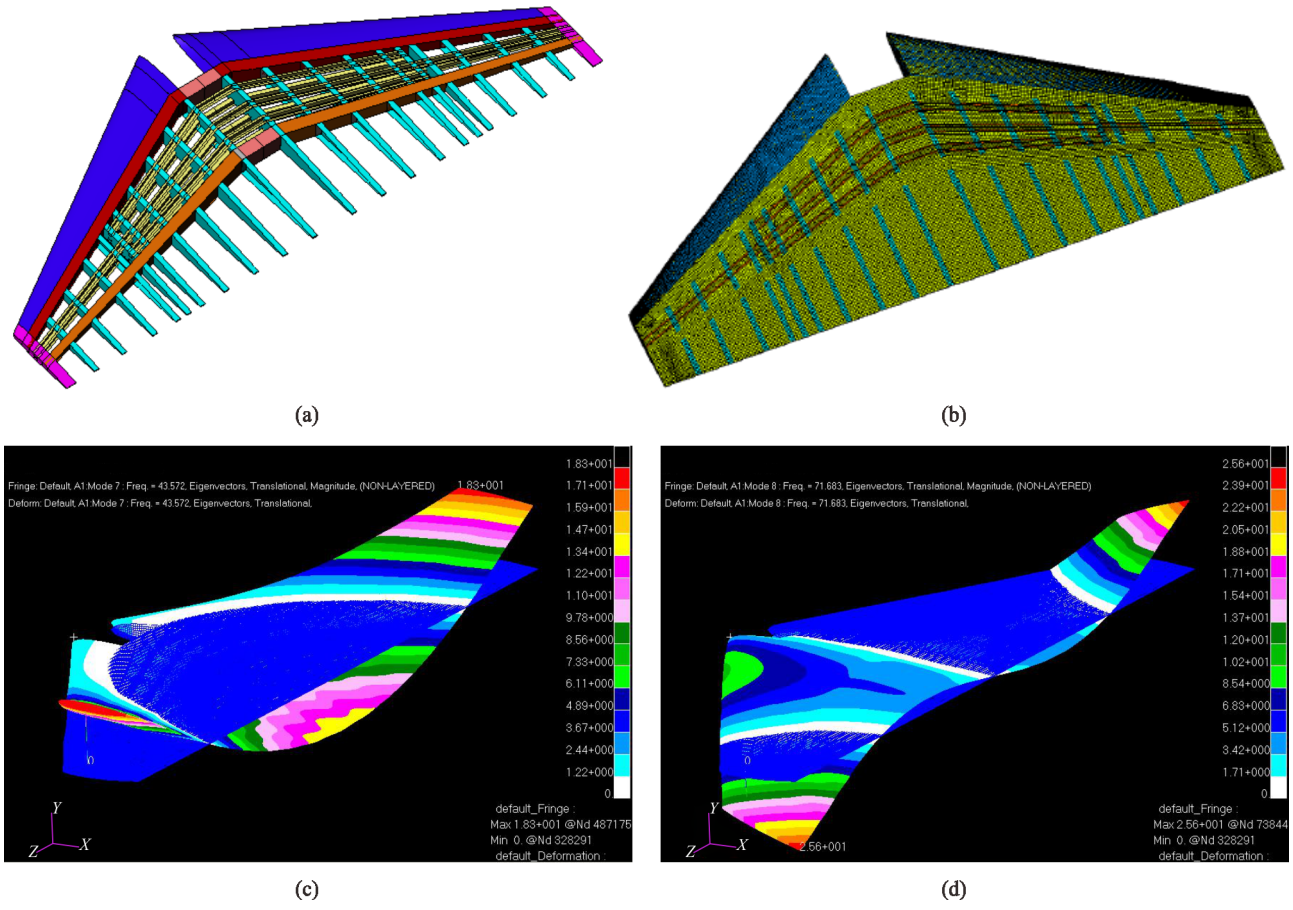

Fig. 13 (a) Three dimensional solid model and the (b) finite element meshed model of the composite wing structure. Deformed configurations at the (c) First and the (d) second natural frequencies, 43.57 Hz and 71.68 Hz, respectively

maximum values of the trailing edge displacement and the von-Mises stress are observed to 7.72 mm and 198 MPa, respectively, occurred at 50 N load case.

4.3 Example 3: auxetic structure with circular cells

The third example is on the design and analysis of AACC as shown in Fig. 11(b). Figure 12(b) shows the FE model of the AACC. We consider the same geometry and material properties of the airfoil as in example 2, except that the cells are circular. The axial load (P) is applied near the core as a concentrated load as show in Fig. 11(b). The deformed configurations and the distribution of the von-Mises stress at various axial load values are plotted in Fig. 15. Figures 15(a)–(e) shows the deformed configurations and the Figs. 15(f)–(j) shows the distribution of the von-Mises stress at axial loads of 5, 20, 50, 100 and 150 N respectively. The maximum values of the trailing edge displacement and the von-Mises stress are observed to 11.2 mm and 377 MPa, respectively, occurred at 50 N load case. Whereas, the corresponding values with elliptic cells are observed to be 7.72 and 198 MPa, respectively. Therefore, for a given loading conditions, the displacements and stresses in AACC are observed to be large compared to the AAEC.

Comparison of the load-displacement, load-von-Mises stress and von-Mises stress-displacement plots of AAEC and AACC are shown in Fig. 16. The load-displacement behavior is linear, as we adopted the linear analysis. The load displacement curves are validated with the experiment Spadoni and Ruzzene [72] in Fig. 17. The experimental results are captured during the loading and unloading cycles. The numerical results are in close agreement with the experiment.

5 Conclusions

A frame work has been developed to design the structure of an aircraft wing based on the aerodynamics loads. The aerodynamic loads acting on a wing structure are converted to equivalent distributed loads. A methodology has been established to estimate the shear forces and bending and twisting moments along the wing span based on the distributed loads. A frame work has been developed to estimate the sizes of various sections of a wing structure, based on the estimated shear forces and bending and

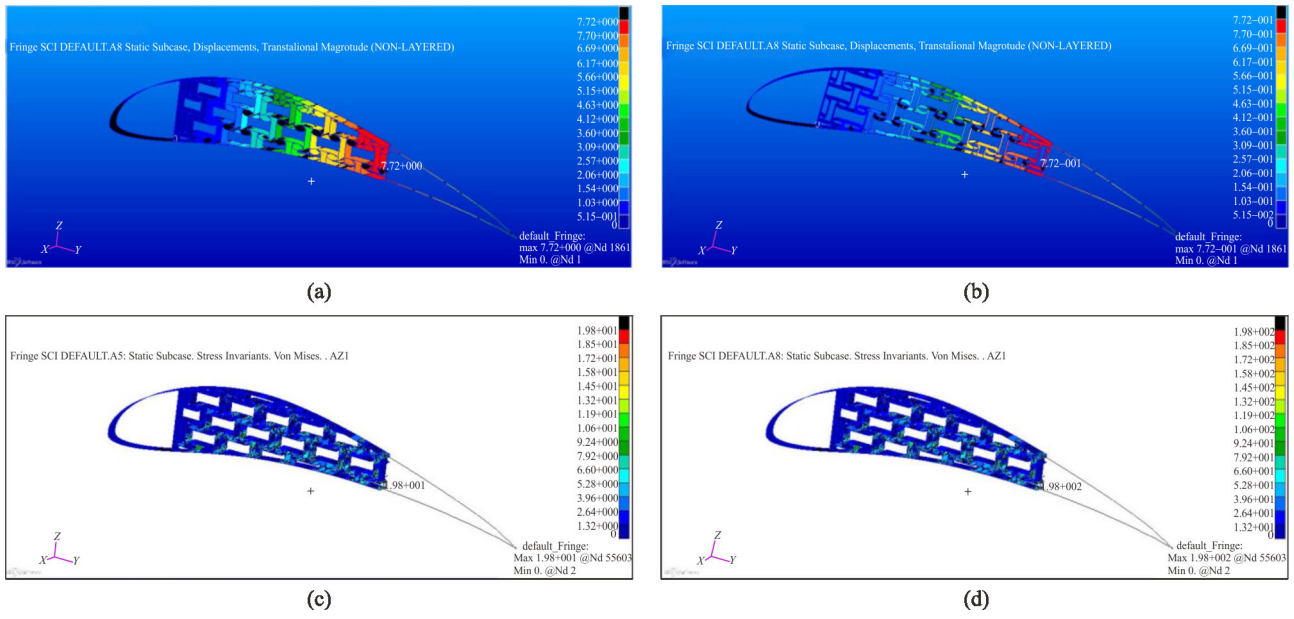

Fig. 14 Deformed configurations of AAEC at axial loads of 5N and 50N are plotted in figures (a) and (b), respectively, and the corresponding distribution of the von-Mises stresses are plotted in (c) and (d), respectively. The maximum amplitude of the displacement and the stress is mentioned in each picture

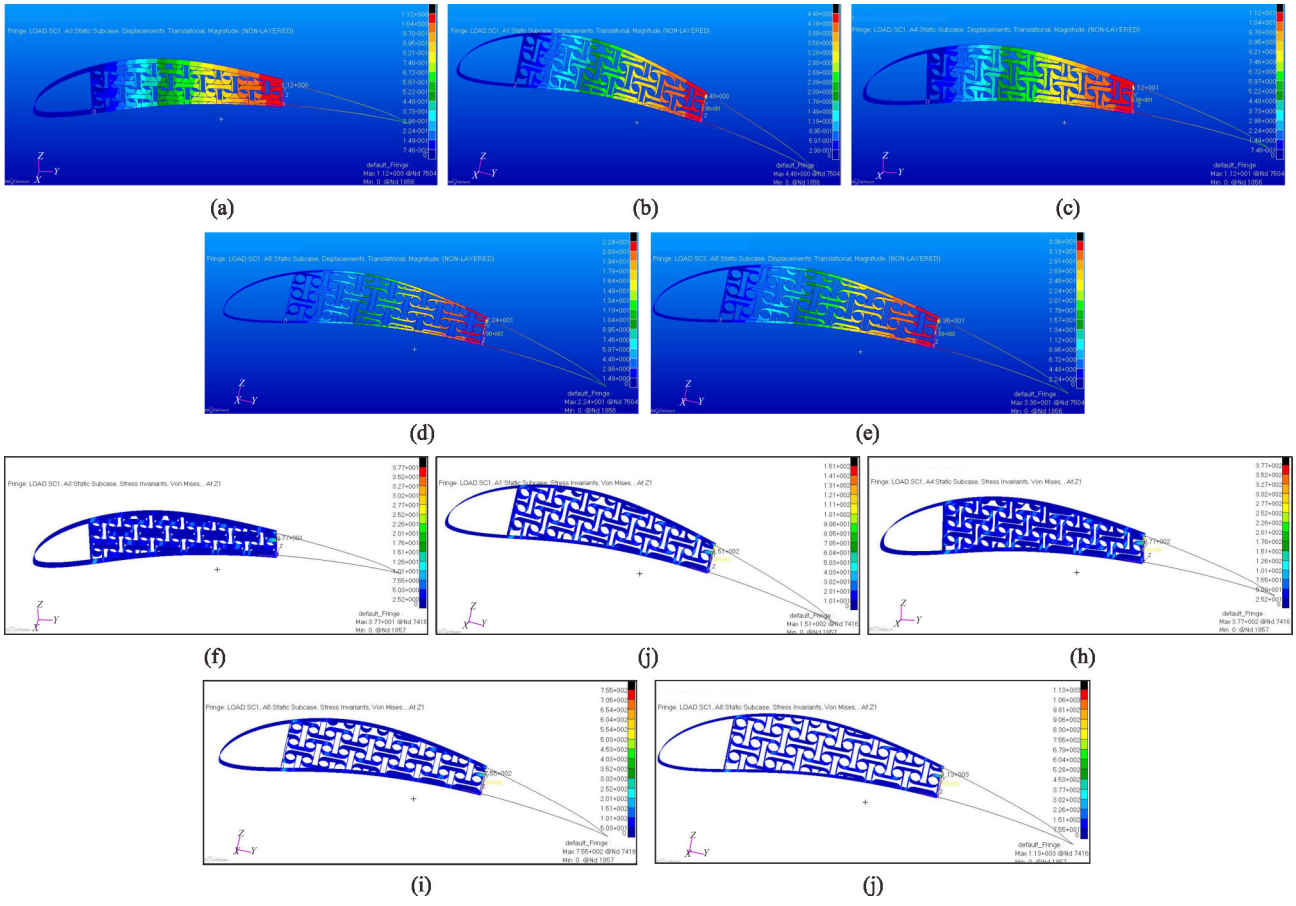

Fig. 15 Deformed configurations of AACC at axial loads of 5N, 20N, 50N, 100N and 150N are plotted in figures (a)–(e), respectively, and the corresponding distribution of the von-Mises stresses are plotted in (f) and (j), respectively. The maximum amplitude of the displacement and the stress is mentioned in each picture

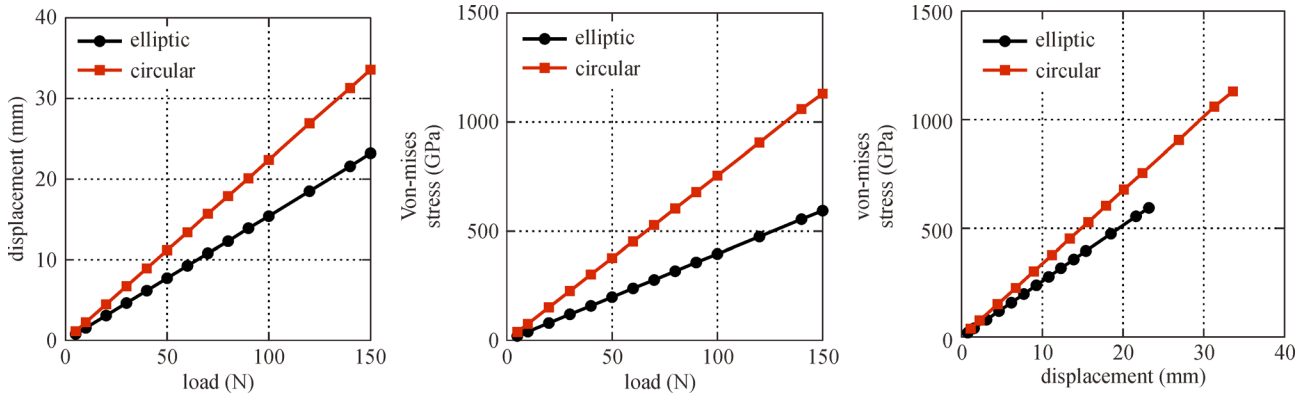

Fig. 16 Comparison of the load-displacement, load-von-Mises stress and von-Mises stress displacement plots of AAEC and AACC

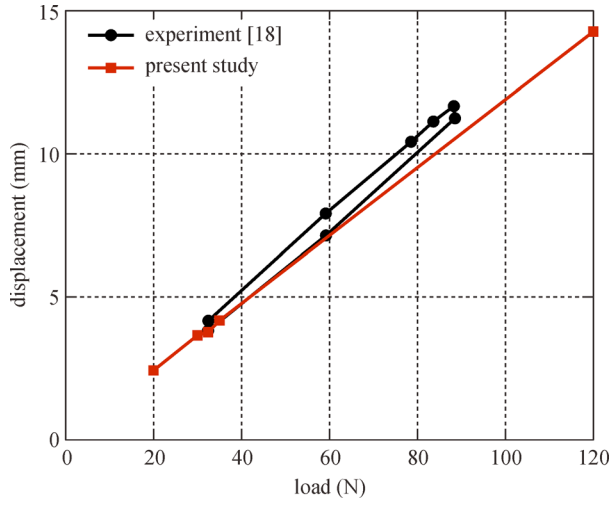

Fig. 17 Validation of the load-displacement plots with the experiment Spadoni and Ruzzene [73]

twisting moments. The design is based on the failure strength. A three dimensional model of the composite wing structure is developed and analyzed for the extreme load conditions. The estimated natural frequencies are observed to be in the acceptable limits.

The properties of auxetic structures for elliptical and circular nodes are investigated. The considered configuration finds potential application as part of a morphing airfoil. We consider the structures with negative Poisson's effect, with circular and elliptical nodes; each node being tangentially connected with four ligaments. The structure deform by the action of node rotation and ligament bending. The proposed design of the auxetic structure is accommodated within the airfoil profile to provide with a chord wise bending compliance, combined with the ability of carrying torsional loads. The compliance characteristics of airfoils with circular and elliptical node designs are investigated. The ability of the structure to undergo large deflections while remaining in the linear range and the influence of the core design on the overall performance of the airfoil are also studied. For a given loading conditions, the displacements and stresses in AACC are observed to be large compared to the AAEC. The load displacement plots are compared with the experimental results. The numerical results closely agree with the experimental results in the literature.

Acknowledgements Sudhir Sastry acknowledges the support of Department of Aeronautical Engineering, Institute of Aeronautical Engineering. Pattabhi Budarapu thankfully acknowledges the financial support from the IRSES.

References

1. Frolov V. Strength of a composite material for structural applications. Mechanics of Composite Materials, 1987, 23(2): 148–154
2. Budarapu P, Narayana T, Rammohan B, Rabczuk T. Directionality of sound radiation from rectangular panels. Applied Acoustics, 2015, 89: 128–140
3. Budarapu P, Rammohan B, Vijay S, Satish B, Raghunathan R. Aero-elastic analysis of stiffened composite wing structure. Journal of Vibration Engineering & Technologies, 2009, 8(3): 255–264
4. Budarapu P R, Yb S S, Javvaji B, Mahapatra D R. Vibration analysis of multi-walled carbon nanotubes embedded in elastic medium. Frontiers of Structural and Civil Engineering, 2014, 8(2): 151–159
5. Benloulo I S, Sánchez-Gálvez V. A new analytical model to simulate impact onto ceramic/composite armors. International Journal of Impact Engineering, 1998, 21(6): 461–471
6. Rawal S. Metal-matrix composites for space applications. Journal of the Minerals Metals & Materials Society, 2001, 53(4): 14–17
7. Tucker V. Gliding birds: the effect of variable wing span. Journal of Experimental Biology, 1987, 133: 33–58
8. Weiss P. Wings of change: shape-shifting aircraft ply future skyways. Science News, 2003, 164(23): 359
9. Lentink D, Mueller U, Stamhuis E, de Kat R, van Gestel W, Veldhuis L, Henningsson P, Hedenstroem A, Videler J, van Leeuwen J. How swifts control their glide performance with morphing wings. Nature, 2007, 446(7139): 1082–1085
10. Parrott G. Aerodynamics of gliding flight of a black vulture coragyps atratus. Journal of Experimental Biology, 1970, 53: 363–

374
11. Newman B. Soaring and gliding flight of the black vulture. Journal of Experimental Biology, 1958, 35: 280–285
12. McGowan A, Washburn A, Horta L, Bryant R. Recent results from nasas morphing project. In: Proceedings of the 9th International Symposium on Smart Structures and Materials. SPIE 4698–11, San Diego, California, 2002
13. Campanile L, Sachau D. The belt-rib concept: a structronic approach to variable camber. Journal of Intelligent Material Systems and Structures, 2000, 11(3): 215–224
14. Monner H, Sachau D, Breitbach E. Design aspects of the elastic trailing edge for an adaptive wing. In: Proceedings of the Research and Technology Organization. ADP010488, Ottawa, 1999, 1–8
15. Bueter A, Ehlert U, Sachau D, Breitbach E. Design aspects of the elastic trailing edge for an adaptive wing. In: Proceeding of RTO symposium on Active Control Technology. ADP011142, Braunschweig, 2000
16. Cadogan D, Smith T, Uhelsky F, MacCusick M. Morphing airfoil wing development for compact package unmanned aerial vehicles. In: Proceedings of the 45th AIAA/ASME/ASCE/AHS/ASC Structures, Structural Dynamics and Materials Conference, AIAA, California, 2004, 3205–3217
17. Bae J, Seigler T, Inman D, Lee I. Aerodynamic and aeroelastic considerations of a variable span morphing wing. In: Proceedings of the 45th AIAA/ASME/ASCE/AHS/ASC. Structural Dynamics and Materials Conference, Aircraft, 2003, 40(4): 734–740
18. Trenker M. Design concepts for adaptive airfoils with dynamic transonic flow control. Journal of Aircraft, 2003, 40(4): 734–740
19. Kudva J. Overview of the darpa smart wing project. Journal of Intelligent Material Systems and Structures, 2004, 15(4): 261–267
20. Spadoni A, Ruzzene M, Scarpa F. Dynamic response of chiral trusscore assemblies. Journal of Intelligent Material Systems and Structures, 2006, 17(11): 941–952
21. Thai C H, Nguyen-Xuan H, Bordas S P A, Nguyen-Thanh N, Rabczuk T. Static, free vibration and buckling analysis of laminated composite reissner-mindlin plates using nurbs-based isogeometric approach. International Journal for Numerical Methods in Engineering, 2012, 91(6): 571–603
22. Nguyen-Xuan H, Nguyen-Thanh N, Bordas S, Rabczuk T. Isogeometric analysis of laminated composite plates using the higher-order shear deformation theory. Mechanics of Advanced Materials and Structures, 2015, 22(6): 451–469
23. Phan-Dao H, Nguyen-Xuan H, Thai-Hoang C, Nguyen-Thoi T, Rabczuk T. An edge-based smoothed finite element method for analysis of laminated composite plates. International Journal of Computational Methods, 2013, 10(1): 1340005
24. Kerfriden P, Schmidt K, Rabczuk T, Bordas S. Statistical extraction of process zones and representative subspaces in fracture of random composites. International Journal for Multiscale Computational Engineering, 2013, 11(3), 253–287
25. Amiri F, Anitescu C, Arroyo M, Bordas S, Rabczuk T. Xlme interpolants, a seamless bridge between xfem and enriched meshless methods. Computational Mechanics, 2014, 53(1): 45–57
26. Amiri F, Millán D, Shen Y, Rabczuk T, Arroyo M. Phase-field modeling of fracture in linear thin shells. Theoretical and Applied Fracture Mechanics, 2014, 69: 102–109
27. Areias P, Rabczuk T. Finite strain fracture of plates and shells with configurational forces and edge rotation. International Journal for Numerical Methods in Engineering, 2013, 94(12): 1099–1122
28. Areias P, Rabczuk T, Camanho P. Initially rigid cohesive laws and fracture based on edge rotations. Computational Mechanics, 2013, 52(4): 931–947
29. Areias P, Rabczuk T, Camanho P. Finite strain fracture of 2d problems with injected anisotropic softening elements. Theoretical and Applied Fracture Mechanics, 2014, 72: 50–63
30. Areias P, Rabczuk T, Dias-da Costa D. Element-wise fracture algorithm based on rotation of edges. Engineering Fracture Mechanics, 2013a, 110: 113–137
31. Belytschko T, Lu Y, Gu L. Element-free galerkin methods. International Journal for Numerical Methods in Engineering, 1994, 37(2): 229–256
32. Bordas S P A, Natarajan S, Kerfriden P, Augarde C E, Mahapatra D R, Rabczuk T, Pont S D. On the performance of strain smoothing for quadratic and enriched finite element approximations (XFEM/GFEM/PUFEM). International Journal for Numerical Methods in Engineering, 2011, 86(4–5): 637–666
33. Bordas S, Rabczuk T, Nguyen-Xuan H, Natarajan S, Bog T, Nguyen V, Do M, Nguyen-Vinh H. Strain smoothing in fem and xfem. Computers & Structures, 2010, 88(23–24): 1419–1443
34. Bordas S, Rabczuk T, Zi G. Three-dimensional crack initiation, propagation, branching and junction in non-linear materials by an extended meshfree method without asymptotic enrichment. Engineering Fracture Mechanics, 2008, 75(5): 943–960
35. Budarapu P, Gracie R, Bordas S, Rabczuk T. An adaptive multiscale method for quasi-static crack growth. Computational Mechanics, 2014, 53(6): 1129–1148
36. Budarapu P, Gracie R, Yang S, Zhuang X, Rabczuk T. Efficient coarse graining in multiscale modeling of fracture. Theoretical and Applied Fracture Mechanics, 2014, 69: 126–143
37. Budarapu P R, Javvaji B, Sutrakar V K, Roy Mahapatra D, Zi G, Rabcz. Crack propagation in graphene. Journal of Applied Physics, 2015, 118(6): 382–395
38. Cai Y, Zhu H, Zhuang X. A continuous/discontinuous deformation analysis (cdda) method based on deformable blocks for fracture modelling. Frontiers of Structural & Civil Engineering, 2013, 7(4): 369–378
39. Cai Y, Zhuang X, Zhu H. A generalized and efficient method for finite cover generation in the numerical manifold method. International Journal of Computational Methods, 2013, 10(5): 1350028
40. Ghorashi S, Valizadeh N, Mohammadi S, Rabczuk T. T-spline based xiga for fracture analysis of orthotropic media. Computers & Structures, 2015, 147: 138–146
41. Liu G, Gu Y T. A local radial point interpolation method (lrpim) for free vibration analyses of 2-d solids. Journal of Sound and Vibration, 2001, 246(1): 29–46
42. Nguyen-Thanh N, Kiendl J, Nguyen-Xuan H, Wuchner R, Bletzinger K, Bazilevs Y, Rabczuk T. Rotation free isogeometric thin shell analysis using pht-splines. Computer Methods in Applied Mechanics and Engineering, 2011, 200(47–48): 3410–3424
43. Rabczuk T, Areias P, Belytschko T. A meshfree thin shell method for nonlinear dynamic fracture. International Journal for Numerical Methods in Engineering, 2007, 72(5): 524–548

44. Rabczuk T, Belytschko T. Cracking particles: a simplified meshfree method for arbitrary evolving cracks. International Journal for Numerical Methods in Engineering, 2004, 61(13): 2316–2343
45. Rabczuk T, Belytschko T. Application of particle methods to static fracture of reinforced concrete structures. International Journal of Fracture, 2006, 137(1–4): 19–49
46. Rabczuk T, Belytschko T. A three dimensional large deformation meshfree method for arbitrary evolving cracks. Computer Methods in Applied Mechanics and Engineering, 2007, 196(29–30): 2777–2799
47. Rabczuk T, Belytschko T, Xiao S. Stable particle methods based on lagrangian kernels. Computer Methods in Applied Mechanics and Engineering, 2004, 193(12–14): 1035–1063
48. Rabczuk T, Bordas S, Zi G. A three-dimensional meshfree method for continuous multiple-crack initiation, propagation and junction in statics and dynamics. Computational Mechanics, 2007, 40(3): 473–495
49. Rabczuk T, Gracie R, Song J, Belytschko T. Immersed particle method for fluidstructure interaction. International Journal for Numerical Methods in Engineering, 2010, 81(1): 48–71
50. Rabczuk T, Samaniego E. Discontinuous modelling of shear bands using adaptive meshfree methods. Computer Methods in Applied Mechanics and Engineering, 2008, 197(6–8): 641–658
51. Rabczuk T, Zi G. A meshfree method based on the local partition of unity for cohesive cracks. Computational Mechanics, 2007, 39(6): 743–760
52. Rabczuk T, Zi G, Bordas S, Nguyen-Xuan H. A geometrically non-linear three dimensional cohesive crack method for reinforced concrete structures. Engineering Fracture Mechanics, 2008, 75(16): 4740–4758
53. Rabczuk T, Zi G, Gerstenberger G, Wall W. A new crack tip element for the phantom node method with arbitrary cohesive cracks. International Journal for Numerical Methods in Engineering, 2008, 75(5): 577–599
54. Talebi H, Silani M, Bordas S, Kerfriden P, Rabczuk T. A molecular dynamics/xfem coupling by a three-dimensional extended bridging domain with applications to dynamic brittle fracture. International Journal for Multiscale Computational Engineering, 2013, 11(6): 527–541
55. Talebi H, Silani M, Bordas S, Kerfriden P, Rabczuk T. A computational library for multiscale modelling of material failure. Computational Mechanics, 2014, 53(5): 1047–1071
56. Talebi H, Silani M, Rabczuk T. Concurrent multiscale modelling of three dimensional crack and dislocation propagation. Advances in Engineering Software, 2015, 80: 82–92
57. Yang S, Budarapu P, Mahapatra D, Bordas S, Zi G, Rabczuk T. A meshless adaptive multiscale method for fracture. Computational Materials Science, 2015a, 96: 382–395
58. Zhuang X, Augarde C, Mathisen K. Fracture modelling using meshless methods and level sets in 3d: framework and modelling. International Journal for Numerical Methods in Engineering, 2012, 92(11): 969–998
59. Zhuang X, Huang R, Zhu H, Askes H, Mathisen K. A new and simple lockingfree triangular thick plate element using independent shear degrees of freedom. Finite Elements in Analysis and Design, 2013, 75: 1–7
60. Zhuang X, Zhu H, Augarde C. An improved meshless shepard and least square method possessing the delta property and requiring no singular weight function. Computational Mechanics, 2014, 53(2): 343–357
61. Zi G, Chen H, Xu J, Belytschko T. The extended finite element method for dynamic fractures. Shock and Vibration, 2005, 12(1): 9–23
62. Ainsworth J, Collier C, Yarrington P, Lucking R, Locke J. Airframe wingbox preliminary design and weight prediction, Society of Allied Weight Engineers, (SAWE), 2010
63. Morishima R. Analysis of composite wing structures with a morphing leading edge, Dissertation for the Doctoral Degree, 2011
64. Arunkumar K, Lohith N, Ganesha B. Effect of ribs and stringer spacings on the weight of aircraft structure for aluminum material. Journal of Applied Sciences, 2012, 12(10): 1006–1012
65. Kennedy G, Martins J. A comparison of metallic and composite aircraft wings using aerostructural design optimization', American Institute of Aeronautics and Astronautics, 2012, 1–31
66. Sudhir Sastry Y B, Budarapu P R, Krishna Y, Devaraj S. Studies on ballistic impact of the composite panels. Theoretical and Applied Fracture Mechanics, 2014, 72: 2–12
67. Sudhir Y, Budarapu P, Madhavi N, Krishna Y. Buckling analysis of thin wall stiffened composite panels. Computational Materials Science, 2015a, 96B: 459–471
68. Sudhir Y, Krishna Y, Budarapu P. Parametric studies on buckling of thin walled channel beams. Computational Materials Science, 2015b, 96B: 416–424
69. Jones R. Mechanics of composite materials, Taylor and Francis, 1999
70. Reddy J. Mechanics of laminated composite plates theory and analysis, CRP press, 1997
71. Prall D, Lakes R. Properties of a chiral honeycomb with a poissons ratio of −1. International Journal of Mechanical Sciences, 1997, 39 (3): 305–314
72. Spadoni A, Ruzzene M. Numerical and experimental analysis of the static compliance of chiral truss-core airfoils. Journal of Mechanics of Materials and Structures, 2007, 2(5): 965–981